JOURNAL OF GEOPHYSICAL RESEARCH, VOL. 95, NO. D6, PAGES 7637–7652, MAY 20, 1990

Interpretation of Ground-Based Radiometric Observations in Terms of a Gravity Wave Model

F. G. CANAVERO

Dipartimento di Elettronica, Politecnico of Turin, Italy

F. EINAUDI

Laboratory for Atmospheres, NASA Goddard Space Flight Center, Greenbelt, Maryland

E. R. WESTWATER, M. J. FALLS, J. A. SCHROEDER, AND A. J. BEDARD, JR.

Wave Propagation Laboratory, NOAA, Boulder, Colorado

An analysis is presented of 2-hour and 4-hour segments of data taken at Denver, Colorado, on February 3, 1984, by a ground-based radiometer designed and operated by the Wave Propagation Laboratory of the National Oceanic and Atmospheric Administration (NOAA). The zenith-viewing instrument has two moisture-sensing and four temperature-sensing channels. It is demonstrated that a peak at a period of 10 min, present in the spectra of the measured brightness temperature and of the derived geopotential heights, thicknesses, and vertically integrated water vapor content, is due to an internal gravity wave generated by wind shear in the jet aloft. This analysis shows that the radiometer has the sensitivity to detect such disturbances and that the mathematical inversion technique used to retrieve the geopotential field and other integrated quantities retains the derived information as well. Finally, a linear expression is derived which relates the brightness temperature to the atmospheric temperature, density, humidity, and cloud liquid perturbation fields.

1. INTRODUCTION

A major effort is under way to develop and test remote-sensing systems to measure tropospheric wind, temperature, and humidity. These systems, often referred to as profilers, employ radiometric and Doppler radar technology [*Hogg et al.*, 1983*a*]. They have the capability of affecting research activities and operational applications substantially. This capability is especially important in mesoscale meteorology where changes occur more rapidly than those resolved by the standard rawinsonde data [*Augustine and Zipser*, 1987]. Further references on the wind measurements are given by *Balsley and Gage* [1982] and by *Strauch et al.* [1984]; remote sensing of temperature profiles is discussed by *Westwater et al.* [1985].

We limit our attention to the passive microwave radiometer developed by the Wave Propagation Laboratory (WPL) of NOAA and located near Stapleton Airport in Denver, Colorado. It uses six channels, two operating near 20 and 30 GHz and four operating between 50 and 60 GHz, to measure downwelling thermal radiation emitted by the atmosphere. Both absolute and relative accuracy of the instrument are good. The absolute accuracy, as determined by an independent calibration standard, is 0.5 K; the ability of the instrument to respond to short-term changes, the sensitivity, is about 0.1 K. From the instrumental measurements, information on temperature and moisture is derived by a mathematical inversion procedure [*Strand and Westwater*, 1968]. The errors in the derived quantities, such as temperature and water vapor, are related to errors in the measured brightness temperature in a straightforward, but complicated, manner [*Strand and Westwater*, 1968]. Although the accuracy of the derived temperature profiles decreases with height, the differences with the rawinsonde-measured temperatures remain quite small for the 700- and 500-mb levels. The vertical resolution, on the other hand, is insufficient to reproduce elevated inversions. Additional information on the instrument and its performance can be found in *Hogg et al.* [1983*a*]. Further improvement of the overall performance of the ground-based remote-sensing system can be obtained by combining its observations with those from a satellite-based Microwave Sounding Unit (MSU). This point is discussed by *Westwater et al.* [1985] in a paper that also provides a statistical analysis of the performance of such systems based on 460 profiles jointly obtained by the ground-based radiometer, the satellite-based MSU, and rawinsondes.

Although the potential of ground-based radiometers has been under investigation for several years, the exploration of the full capabilities of the system is still in progress. Recent work by *Ciotti et al.* [1987] demonstrates the ability of the instrument to analyze such diverse geophysical situations as the passage of a cold-frontal system and the occurrence of gravity waves. In particular, gravity waves have been shown to influence radiometric measurements in a number of studies (see, for example, *Beard and Martin* [1978], *Decker et al.* [1981], *El-Raey* [1982], and *Hines and Tarasick* [1987] and references therein).

In this paper we analyze one of these gravity wave events in detail. Through the use of an analytical-numerical model, we interpret the radiometric measurements in terms of an internal gravity wave generated by wind shear within the jet. We show that the brightness temperature measurements and derived quantities, such as surfaces of constant pressure and

Paper number 89JD03475.
0148-0227/90/89JD-03475$05.00

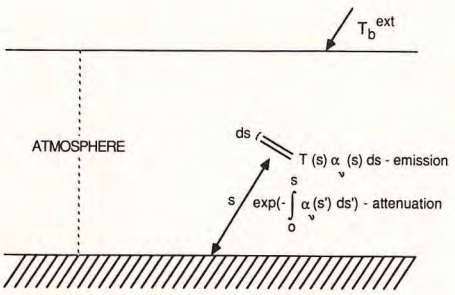

Fig. 1. Geometrical definition of the radiative transfer problem. See text for definition of symbols.

atmospheric thicknesses below 500 mb, have the proper amplitudes as predicted by gravity wave theory. Thus we confirm experimental evidence about the capabilities of the thermodynamic profiler to measure variations of integrated atmospheric variables accurately, and we demonstrate that a substantial depth of the troposphere can be affected by an internal gravity wave.

Microwave radiative transfer is outlined in section 2.1, which is followed by a discussion of linear wave theory in section 2.2. The observations and the results are discussed and interpreted in section 3.

2. Theoretical Model

2.1. *Microwave Radiative Transfer*

Remote sensing by passive radiometric techniques uses the measurement of thermal emission from natural sources of incoherent electromagnetic radiation to infer the temperature and composition of the atmosphere. The basic quantity measured by a radiometer is the average spectral power incident on its antenna. Ground-based remote-sensing radiometers use antennas that accept radiation from only a narrow cone of solid angles, typically 1°–5°. Furthermore, microwave receiver technology allows almost monochromatic radiation to be observed. Typical bandwidths are less than 1% of the center frequency.

To derive the radiative transfer equation relating the measured power to the properties of the medium, a number of simplifying assumptions are made. The atmosphere is considered to be a continuous spatial distribution of all its constituents. Any parcel of air is assumed to be homogeneous and in local thermodynamic equilibrium (i.e., the molecular distribution among the different energy levels obeys Boltzmann's Law, and a local temperature can be defined). Moreover, the absence of scattering processes is assumed; this means that the size of the largest particles must be negligible with respect to the wavelengths at which the measurements are made. For wavelengths less than 0.5 cm (60 GHz), this latter condition may be violated for some types of rain.

Under these assumptions, any elementary volume of air is related to a blackbody; that is, a body which, by Kirchhoff's Law, absorbs all impinging radiation. Furthermore, its emission is due to the thermal agitation and obeys Planck's Law. The power measured by an upward-looking radiometer can then be expressed as the sum of two contributions. The first one, the so-called cosmic term, accounts for the radiation of outer space reduced by the attenuation due to the propagation through the entire atmosphere. The second one is the atmospheric term and accounts for the emission arising from the atmosphere itself (Figure 1).

In the microwave frequency range (1–100 GHz), the Rayleigh-Jeans (RJ) approximation to the Planck function $B_\nu(T)$ is valid and

$$B_\nu(T) = 2\frac{\nu^2}{c^2}\kappa T \tag{1}$$

where ν is the frequency, c is the speed of light, κ is the Boltzmann constant, and T is the absolute temperature. Equation (1) states that the microwave spectral power emitted from a blackbody is directly proportional to its temperature. Consequently, the measured spectral power can be expressed as an equivalent blackbody temperature $T_{b\nu}$. With the RJ approximation, the well-known radiation transfer equation [see *Ulaby et al.*, 1981; *Liou*, 1980] for the brightness temperature measured at the ground can be written as

$$T_{b\nu} = T_b^{ext} \exp\left[-\tau_\nu(0, \infty)\right] + \int_0^\infty T(s)\alpha_\nu(s) \exp\left[-\tau_\nu(0, s)\right] ds \tag{2}$$

where the integral extends over the path s of the radiation. T_b^{ext} describes the cosmic background radiation external to the Earth's atmosphere. The optical depth $\tau_\nu(0, s)$ is related to the absorption coefficient α_ν by

$$\tau_\nu(0, s) = \int_0^s \alpha_\nu(s')\, ds' \tag{3}$$

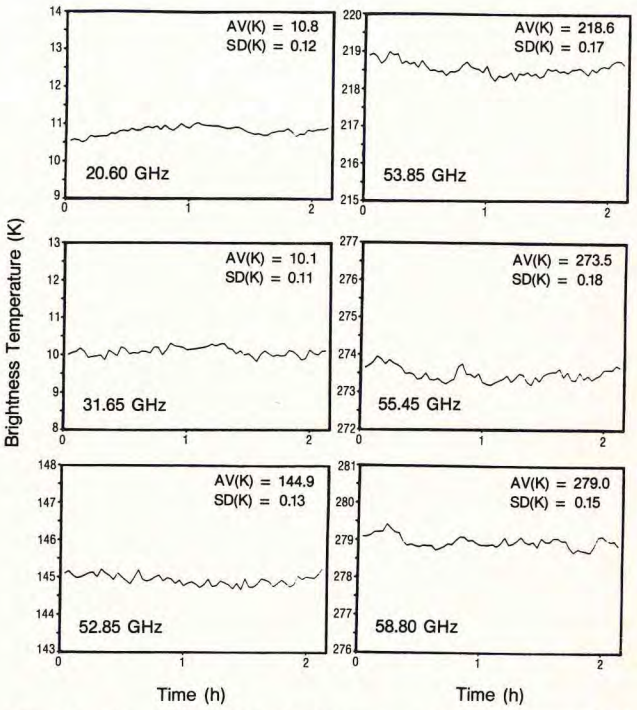

Fig. 2. Time series of the brightness temperature measured at six different frequencies. The observation period started at 1200 UTC February 3, 1984, and lasted 128 min. The different ranges on the vertical axis are explained by the different amounts of radiation collected by the radiometer at the various frequencies. AV and SD refer to average and standard deviation.

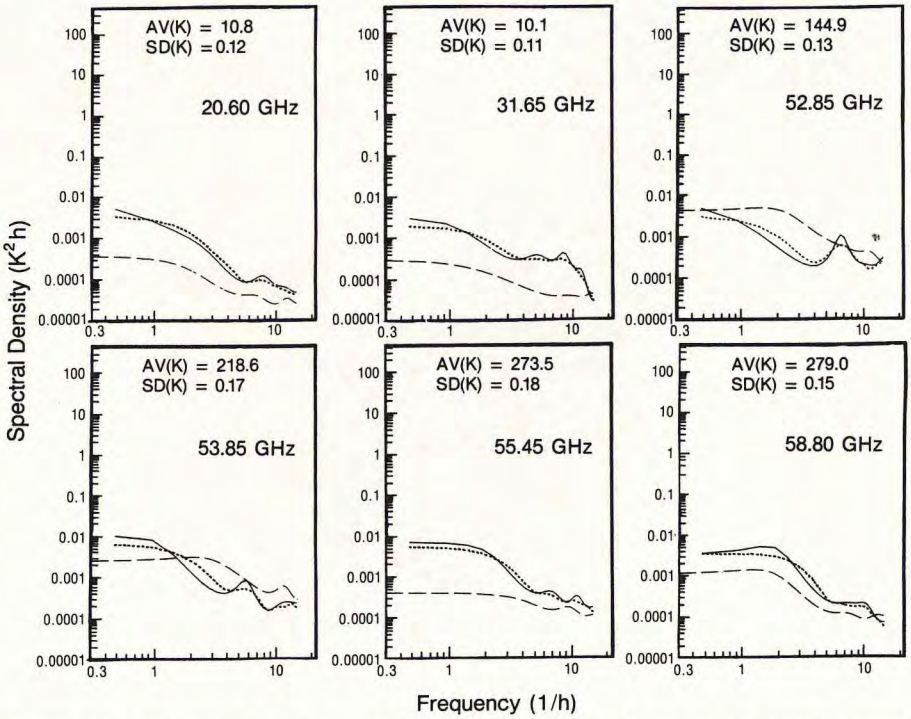

Fig. 3. Spectra of the brightness temperature fluctuations measured by the radiometer at six different frequencies. The observation period started at 1200 UTC February 3, 1984, and lasted 128 min. Two different methods of spectral analysis were used. The dotted line shows the results of the Fourier transform technique with a 16-sample moving average, and the solid line refers to an autoregressive process of order 8. The dashed line indicates the estimated noise level of the instrument. AV and SD are defined in the caption of Figure 2.

The coefficient α_ν accounts for the absorption (and the emission, according to Kirchhoff's Law) of photons by the atmosphere. In the microwave range, water vapor contributes to the absorption spectrum with the electric dipole rotation line at 22.235 GHz and with the wing of strong infrared lines. The oxygen contribution is due to a band of magnetic dipole transitions centered at a frequency of 60 GHz and approximately 20 GHz wide. The absorption coefficient depends on the frequency ν, the temperature T, the dry air density ρ_d, the density of water vapor ρ_v, and the density of cloud liquid water ρ_c:

$$\alpha_\nu = f(\nu;\, T,\, \rho_d,\, \rho_c) \tag{4}$$

The dependence of α_ν on the density of oxygen is accounted for through its dependence on ρ_d. Absorption from liquid-bearing clouds ρ_c can be modeled if the vertical distribution of cloud liquid density is known. For the explicit form of the function f, usually quite complicated, the reader is referred to the papers by *Liebe* [1981] and *Hogg et al.* [1983*b*]. It is worth noting that absorption is a local property of the atmosphere through its dependence on the temperature and composition.

Equation (2) relates the measured brightness temperature to the spatial variation of the atmospheric variables. Temporal variations of these variables can be observed by a microwave radiometer, provided that its integration time is short with respect to the characteristic time of the fluctuations and that the spatial variations are not averaged out in the vertical integration.

To trace the origin of the temporal fluctuations often observed in radiometric measurements, we linearize the radiative transfer equation (2). This linearization is based on the assumption that each atmospheric variable can be expanded as the sum of two terms:

$$a(x,\, z,\, t) = \bar{a}(z) + a'(x,\, z,\, t) \tag{5}$$

where a is a generic variable that may represent the pressure p, the temperature T, the dry density ρ_d, the wet density ρ_v,

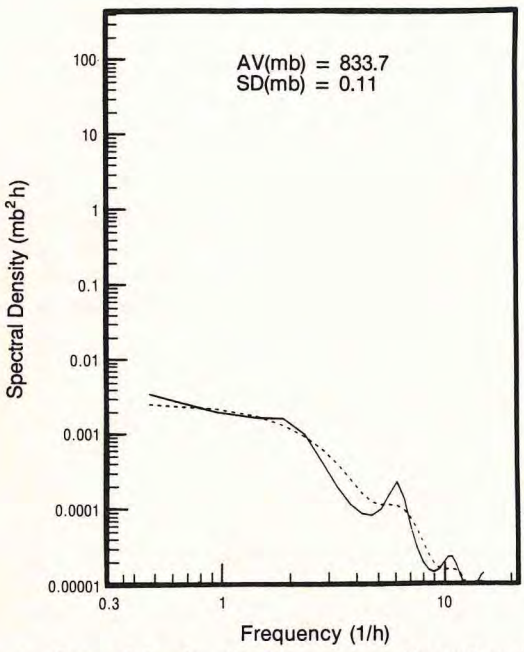

Fig. 4. Spectral density of surface pressure fluctuations for the time interval of the radiometric measurements (1200–1408 UTC February 3, 1984). The two curves represent different spectral analysis techniques, as in Figure 3. AV and SD are defined in the caption of Figure 2.

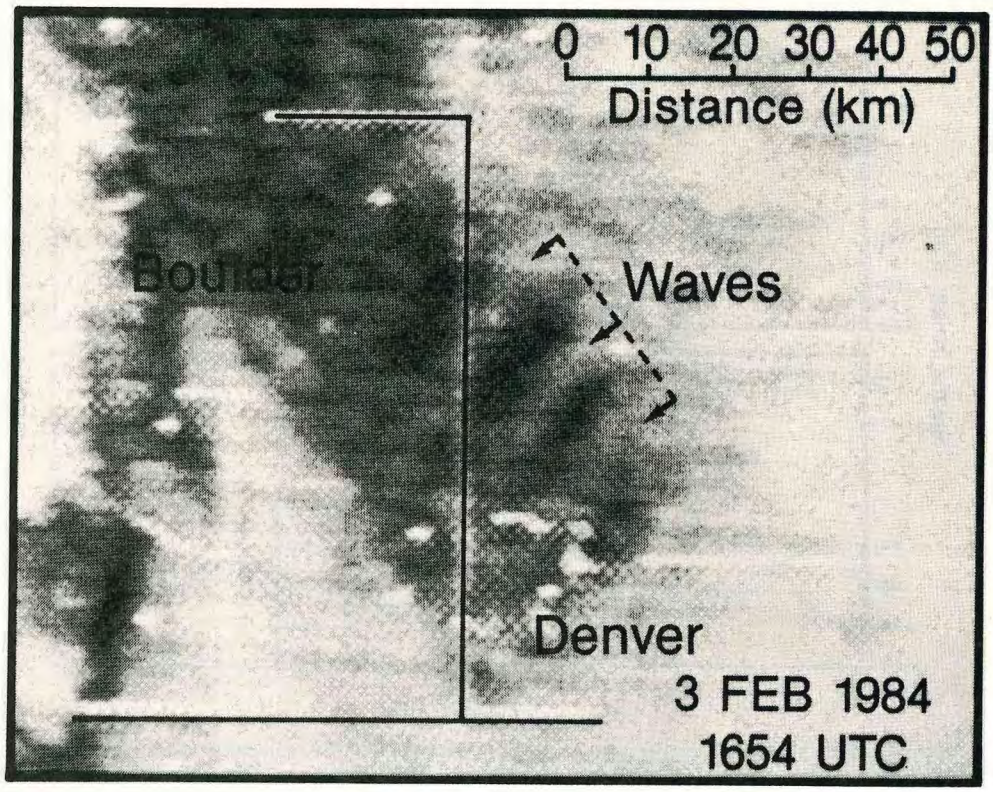

Fig. 5*a*. Segment of GOES east visible satellite photograph for 1654 UTC on February 3, 1984, with key features and a wave train identified. This is one of a series of rapid scan segments showing regional wave activity.

the cloud liquid density ρ_c, and the wind components u and w. In addition, x and z are horizontal and vertical coordinates, and t is time. The motivation for the splitting of (5) is that the atmosphere can very often be described by the superposition of two regimes. The gross, essentially horizontally homogeneous features of the atmosphere are represented by an unperturbed time-independent background state that is taken into account by the $\bar{a}$-type terms. On the other hand, the a'-type term describes a smaller spatial and temporal perturbation superimposed on the average state, such that

$$|a'| \ll |\bar{a}| \tag{6}$$

Using a Taylor expansion, we can write the absorption coefficient at each level as

$$\alpha_\nu = \alpha_\nu(\nu; \bar{T} + T', \bar{\rho}_d + \rho_d', \bar{\rho}_v + \rho_v', \bar{\rho}_c + \rho_c') = \bar{\alpha}_\nu + \alpha_\nu' + \text{higher-order terms} \tag{7}$$

where

$$\bar{\alpha}_\nu = \alpha_\nu(\nu; \bar{T}, \bar{\rho}_d, \bar{\rho}_v, \bar{\rho}_c) \tag{8}$$

$$\alpha_\nu' = \left(\frac{\partial \alpha_\nu}{\partial T}\right) T' + \left(\frac{\partial \alpha_\nu}{\partial \rho_d}\right) \rho_d' + \left(\frac{\partial \alpha_\nu}{\partial \rho_v}\right) \rho_v' + \left(\frac{\partial \alpha_\nu}{\partial \rho_c}\right) \rho_c' \tag{9}$$

where the partial derivatives are calculated for the mean state $T = \bar{T}$, $\rho_d = \bar{\rho}_d$, $\rho_v = \bar{\rho}_v$ and $\rho_c = \bar{\rho}_c$.

Neglecting higher-order terms, we show in Appendix A that the brightness temperature measured at the ground and given by (2) can be written as the sum of two terms:

$$T_{b\nu} = \bar{T}_{b\nu} + T_{b\nu}' \tag{10}$$

where

$$\bar{T}_{b\nu} = T_b^{(\text{ext})} \exp\left[-\bar{\tau}_\nu(0, \infty)\right] + \int_0^\infty \bar{T}(s)\bar{\alpha}_\nu(s) \exp\left[-\bar{\tau}_\nu(0, s)\right] ds \tag{11}$$

is the average value and

$$T_{b\nu}' = \int_0^\infty \left[W_T(s)T'(s) + W_{\rho_d}(s)\rho_d'(s) + W_{\rho_v}(s)\rho_v'(s) + W_{\rho_c}(s)\rho_c'(s)\right] ds \tag{12}$$

is its perturbation part. The latter is given by the integration, along the direction viewed by the radiometer, of the linear combination of T', ρ_d', ρ_v', and ρ_c' whose coefficients $W_T(s)$, $W_{\rho_d}(s)$, $W_{\rho_v}(s)$, and $W_{\rho_c}(s)$ are the temperature, dry air density, water vapor density, and cloud liquid density

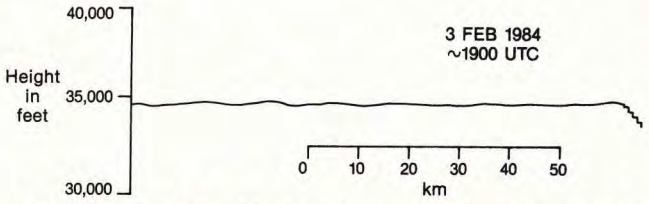

Fig. 5*b*. Plot of the altitude of a segment of the flight path of the National Center for Atmospheric Research Sabreliner aircraft as a function of time, with data points taken every 1 second. We applied microbarograph array data for azimuth in guiding the aircraft to fly along the direction of propagation of the waves. Altitude deviations of several hundred feet are evident at wavelengths also observed by satellite.

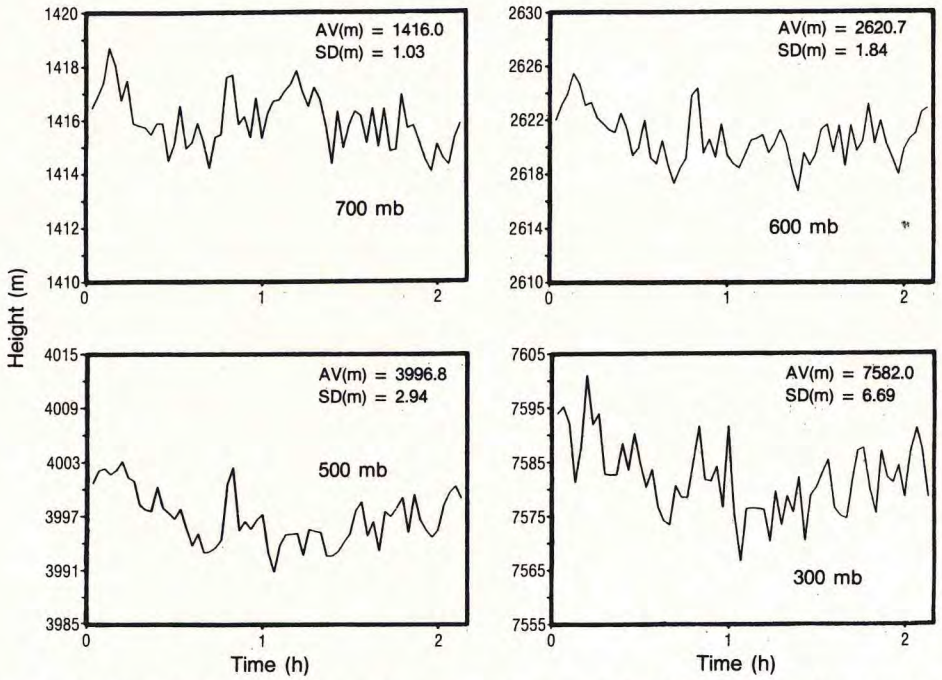

Fig. 6. Time series of the heights of constant pressure surfaces, as derived from radiometric measurements of the dry density. Note that the ordinate scale changes for different heights. AV and SD are defined in the caption of Figure 2.

weighting functions. These functions are derived in Appendix A and depend on the background atmospheric state only. They are plotted as a function of height in Figure A1 from a 10-year climatological mean for the months of December, January, and February at Denver, Colorado. These functions are shown primarily to illustrate the sensitivity of the brightness temperature to various atmospheric parameters. In fact, when we made the model calculations we used the full radiative transfer equations (2) with the mean and the fluctuating quantities provided by the rawinsonde and the wave model calculations, respectively. No liquid water was included since no information was available on its vertical distribution. Liquid water corrections to the brightness temperature calculations were performed in a second stage as discussed later.

The perturbation functions T', ρ_d', ρ_v', and ρ_c' that appear in (12) are quite arbitrary and are, in general, functions of spatial coordinates and time. In section 2.2, we consider the case where they are coherent manifestations of an internal gravity wave generated by vertical shear in the background wind.

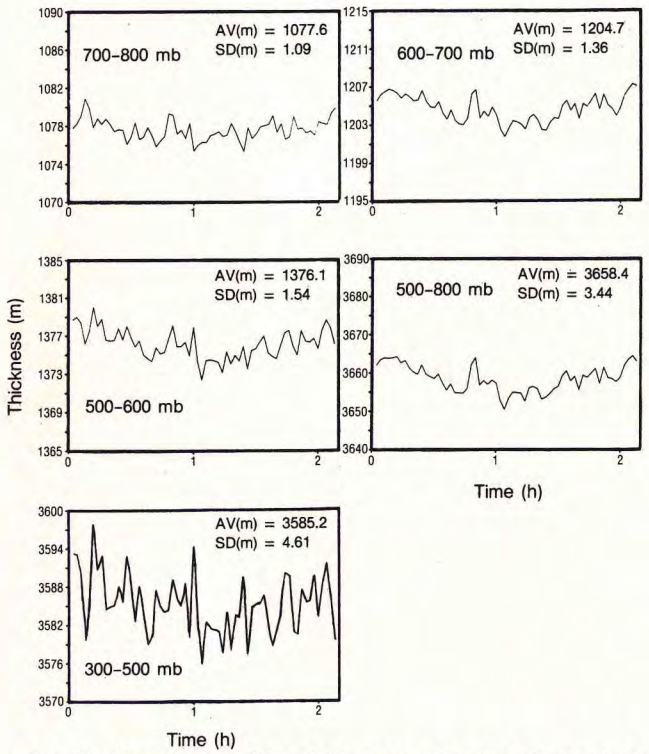

Fig. 7. Time series of the thicknesses of various atmospheric layers, as derived from radiometric measurements. The ordinate scale varies. AV and SD are defined in the caption of Figure 2.

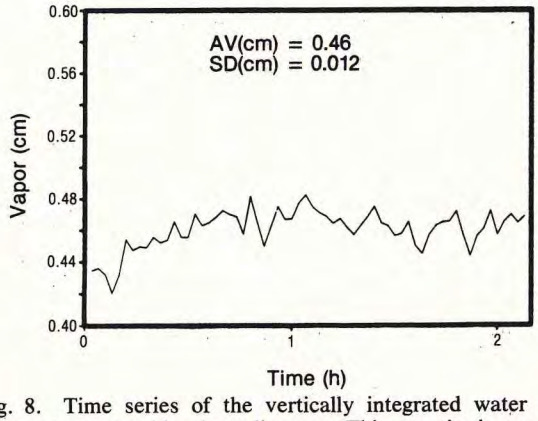

Fig. 8. Time series of the vertically integrated water vapor content, as measured by the radiometer. This quantity is expressed as the depth (in centimeters) of the equivalent layer of water obtained by the condensation of all the vapor aloft. AV and SD are defined in the caption of Figure 2.

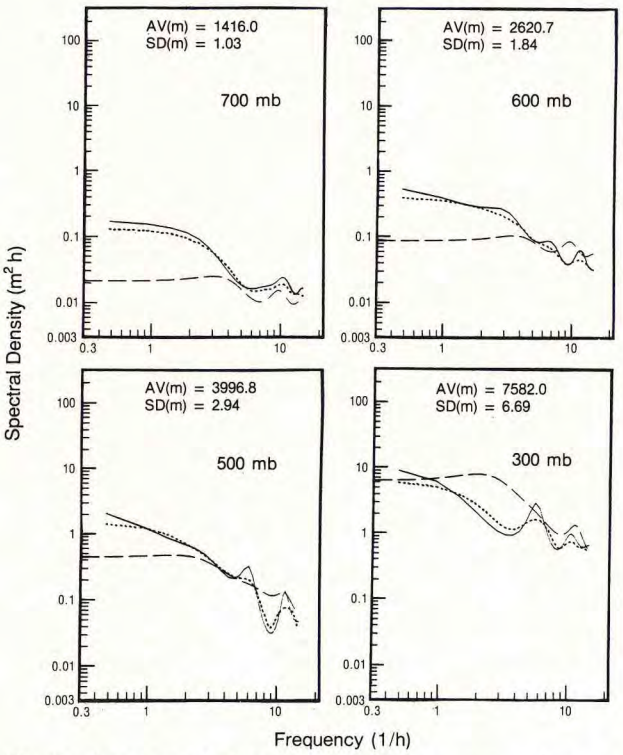

Fig. 9. Spectra of the heights of constant pressure surfaces, as derived from radiometric measurements. Refer to Figure 3 for the identification of the curves. AV and SD are defined in the caption of Figure 2.

2.2. *Gravity Wave Model*

Gravity waves are reversible motions of the atmosphere in which the various quantities such as pressure, density, velocity, and temperature all vary coherently as a function of time and spatial coordinates. The characteristics of the disturbance, horizontal wavelength, period, and vertical structure will be imposed by the mean properties of the atmosphere, that is, its wind and temperature distributions. The range of periods and wavelengths covered by these motions makes it possible for them to be detected by radiometric measurements.

For such motions, the main restoring force is gravity, as opposed to acoustic waves whose restoring force is largely the pressure gradient. At frequencies and wavelengths of interest here, these coherent disturbances must satisfy the equation of motion in a stratified atmosphere in which the rotational effects, heat conduction, and viscosity are neglected.

The atmosphere, when saturated, can be considered as a mixture of three fluids, dry air, water vapor, and water droplets. In particular, terms involving the production of water vapor per unit volume and unit time appear in the conservation of mass equations for water vapor and water droplets and the equation of conservation of energy [see *Einaudi and Lalas*, 1973; *Lalas and Einaudi*, 1973]. In this paper we will assume that the properties of the gravity wave are dictated by the dry air component of the mixture. The time interval, from 1200 to 1408 UTC February 3, 1984, chosen for detailed analysis of wave activity, corresponds to a typical cold winter condition in Denver, Colorado, when the atmosphere is quite dry. This is confirmed by the profiles of temperature and dew point temperature displayed in Figure 12 and by the low values of total water vapor content shown in Figure 8. The total liquid water content, not shown here, is also low during this interval, 2.0×10^{-3} mm. This is less than 50% of the value of 3.3×10^{-3} mm for the longer interval 1040–1448 UTC.

The model equations satisfying the above assumptions are supplied in a two-dimensional orthogonal coordinate system (x, z) where x is the coordinate in the direction of wave

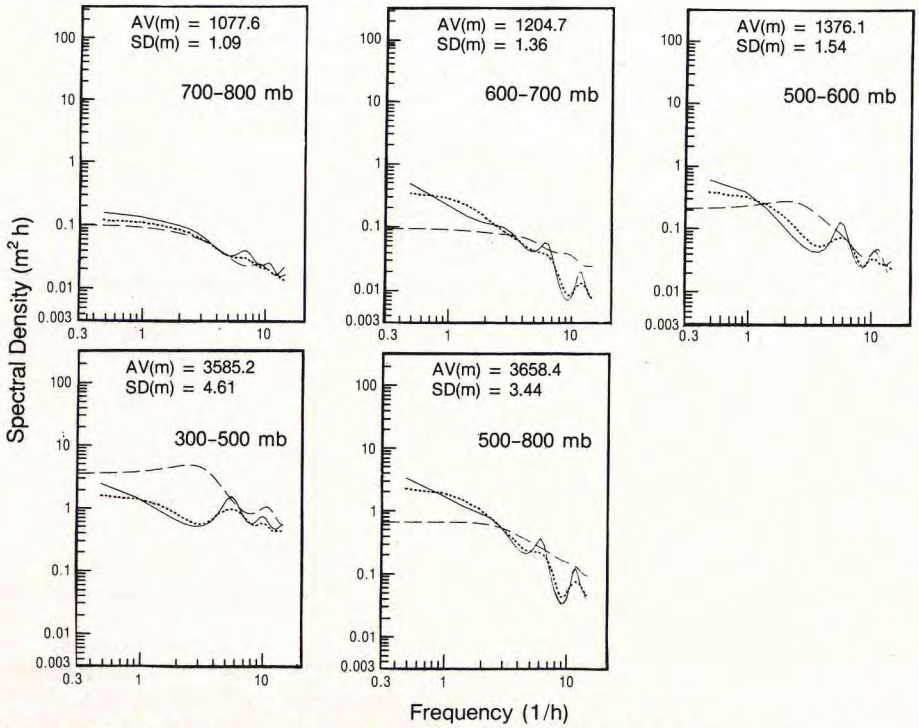

Fig. 10. Spectra of the thicknesses of various atmospheric layers, as derived from radiometric measurements. Refer to Figure 3 for the identification of the different curves. AV and SD are defined in the caption of Figure 2.

propagation and z is the vertical coordinate positive upwards.

The conservation of momentum is given by

$$\rho_d \frac{d\mathbf{v}}{dt} = -\nabla p - \rho_d \mathbf{g} \tag{13}$$

where $\mathbf{v} = u\hat{x} + w\hat{z}$ is the wind vector, p is the partial pressure for dry air, $\mathbf{g}$ represents gravity, $d/dt = \partial/\partial t + \mathbf{v} \cdot \nabla$ indicates the substantial derivative with respect to time, and $\nabla = \partial/\partial x\, \hat{x} + \partial/\partial z\, \hat{z}$. Finally, $\hat{x}$ and $\hat{z}$ are unit vectors in the x and z directions.

The conservation of mass is assumed to hold separately for the dry and wet parts of the atmosphere:

$$\frac{d\rho_d}{dt} + \rho_d \nabla \cdot \mathbf{v} = 0 \tag{14}$$

$$\frac{d\rho_v}{dt} + \rho_v \nabla \cdot \mathbf{v} = 0 \tag{15a}$$

$$\frac{d\rho_c}{dt} + \rho_c \nabla \cdot \mathbf{v} = 0 \tag{15b}$$

Equation (15) implies that changes of state are neglected as discussed above. While the temperatures of dry air and water vapor are the same, the partial pressures (p for dry air and e for water vapor, with $p_{\text{tot}} = p + e$) satisfy the ideal gas law; that is,

$$p = R_d \rho_d T \tag{16}$$

$$e = R_v \rho_v T \tag{17}$$

where R_d and R_v are the gas constants for dry air and water vapor, respectively.

The conservation of energy implies that

$$\frac{d\theta}{dt} = 0 \tag{18}$$

where $\theta = T(p_{\text{ref}}/p)^{R_d/c_p}$ is the potential temperature of a volume of dry air. The quantity $p_{\text{ref}} = 1000$ mb is a reference pressure and c_p is the specific heat at constant pressure.

Equations (13)–(18) contain various nonlinear terms that are very difficult to treat analytically. Therefore we linearize the equations in the manner outlined in section 2.1. The decomposition given in (5), when introduced into (13)–(18), leads to the following set of linearized equations for the perturbation quantities

$$\frac{\partial \rho_d'}{\partial t} + \bar{u}\frac{\partial \rho_d'}{\partial x} + w'\frac{d\bar{\rho}_d}{dz} + \bar{\rho}_d\left(\frac{\partial u'}{\partial x} + \frac{\partial w'}{\partial z}\right) = 0 \tag{19}$$

$$\frac{\partial \rho_v'}{\partial t} + \bar{u}\frac{\partial \rho_v'}{\partial x} + w'\frac{d\bar{\rho}_v}{dz} - \frac{\bar{\rho}_v}{\bar{\rho}_d}\left(\frac{\partial \rho_d'}{\partial t} + \bar{u}\frac{\partial \rho_d'}{\partial x} + w'\frac{d\bar{\rho}_d}{dz}\right) = 0 \tag{20a}$$

$$\frac{\partial \rho_c'}{\partial t} + \bar{u}\frac{\partial \rho_c'}{\partial x} + w'\frac{d\bar{\rho}_c}{dz} - \frac{\bar{\rho}_c}{\bar{\rho}_d}\left(\frac{\partial \rho_d'}{\partial t} + \bar{u}\frac{\partial \rho_d'}{\partial x} + w'\frac{d\bar{\rho}_d}{dz}\right) = 0 \tag{20b}$$

$$\bar{\rho}_d\left(\frac{\partial u'}{\partial t} + \bar{u}\frac{\partial u'}{\partial x} + w'\frac{d\bar{u}}{dz}\right) = -\frac{\partial p'}{\partial x} \tag{21}$$

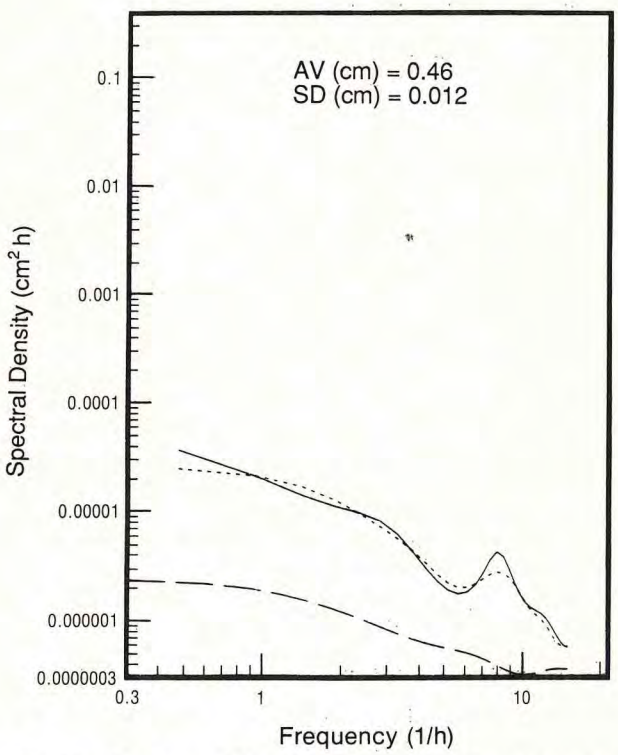

Fig. 11. Spectrum of the vertically integrated water vapor content, as measured from the radiometer. Refer to Figure 3 for the identification of the different curves. AV and SD are defined in the caption of Figure 2.

$$\bar{\rho}_d\left(\frac{\partial w'}{\partial t} + \bar{u}\frac{\partial w'}{\partial x}\right) = -\frac{\partial p'}{\partial z} - g\rho_d' \tag{22}$$

$$\frac{\partial p'}{\partial t} + \bar{u}\frac{\partial p'}{\partial x} + w'\frac{d\bar{p}}{dz} = \bar{c}^2\left(\frac{\partial \rho_d'}{\partial t} + \bar{u}\frac{\partial \rho_d'}{\partial x} + w'\frac{d\bar{\rho}_d}{dz}\right) \tag{23}$$

where (19) and (20) are derived from the continuity equations (14) and (15), equations (21) and (22) are from the equation of conservation of momentum, and (23) is from the conservation of energy. Temperature was eliminated from the linearized set with the use of (16) and (17). The parameter $\bar{c}^2 = \gamma R_d \bar{T}$ represents the speed of sound in the air and $\gamma = c_p/c_v$ is the ratio of specific heats at constant pressure and volume.

An additional assumption is now made that the perturbation quantities are sinusoidal waves:

$$a'(x, z, t) = \text{Re}\,(A'(z)e^{i(\omega t - k_x x)}) \tag{24}$$

where Re ( ) indicates the real part of a complex number, $i = (-1)^{1/2}$ is the imaginary unit, $\omega = \omega_r + i\omega_i$ is the complex frequency, and $k_x = 2\pi/\lambda$ is the real horizontal wavenumber and λ is the wavelength. The complex quantity $A'(z)$ represents the vertical structure of the wave.

Equations (19)–(23) form a system of six equations in six unknowns: u', w', ρ_d', p', ρ_v', and ρ_c'. However, the water vapor density ρ_v' and cloud liquid density ρ_c' appear only in (20), which should be viewed simply as relating ρ_v' and ρ_c' to the gravity wave variables. The latter form a system that is independent of the water vapor and cloud liquid components of the mixture as discussed earlier. To solve the system of equations (19), (21), (22), and (23), it is convenient to introduce an auxiliary variable $D'(z)$, whose time derivative is essentially the vertical velocity. In complex notation,

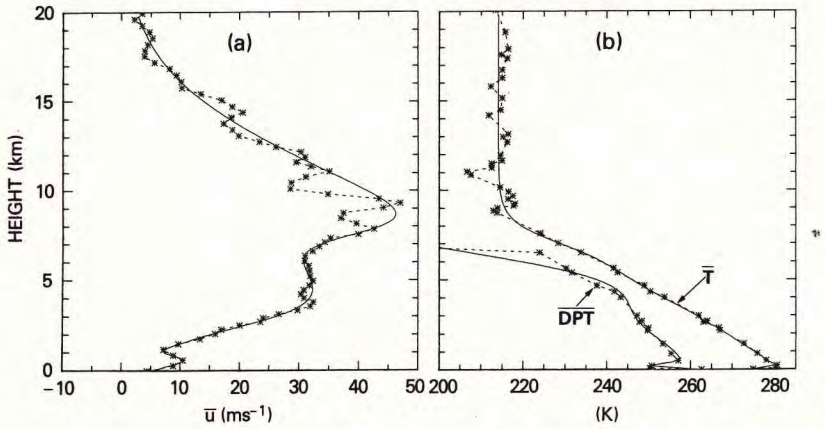

Fig. 12. Rawinsonde data from the launch of 1100 UTC February 3, 1984, from Denver, Colorado, for (*a*) wind and (*b*) temperature and dew point temperature. The winds are projected along the NW direction of 315°. The stars are the data points themselves connected by dashed segments. The solid lines are the best least squares fit using a linear combination of hyperbolic tangent and gaussian functions. The height is above ground level.

$$W'(z) = i\Omega\varepsilon D'(z) \tag{25}$$

where $\Omega = \omega - k_x\bar{u}$ and $\varepsilon = \exp\left[\int^z g/\bar{c}^2(z')\,dz'\right]$. With the help of (24) and (25), one obtains a single second-order ordinary differential equation [*Chimonas*, 1970]:

$$\frac{d}{dz}\left(\frac{r\Omega^2/k_x^2}{1-\Omega^2/(k_x^2\bar{c}^2)}\frac{dD'}{dz}\right) + r(n^2-\Omega^2)D' = 0 \tag{26}$$

where $r = \bar{\rho}_d\varepsilon^2$ and $n^2 = -g[\bar{\rho}_d^{-1}d\bar{\rho}_d/dz + g/\bar{c}^2]$ is the square of the Brunt-Väisälä frequency. The original problem is now reduced to solving (26) for an atmosphere whose background state is specified by the known quantities $\bar{u}(z)$, $\bar{T}(z)$, and $\bar{\rho}_d(z)$. The boundary conditions imply zero vertical displacement at the ground and the radiation condition for $z \to \infty$ [see *Lalas and Einaudi* [1976].

The solution of this Sturm-Liouville problem requires finding the eigenvalues ω and k_x, and the associated eigenfunctions $D'(z)$. Analytical solutions do not exist, except for a very simple background state (e.g., $\bar{u}$ and $\bar{T}$ constant). For more realistic velocity and temperature profiles, one needs to find the solutions numerically; a brief description of our numerical integration scheme is deferred to section 3.

The determination of $D'(z)$ is sufficient for expressing all other perturbation variables, since it can be demonstrated that each quantity is proportional to D' and/or to dD'/dz. As an example, the complex amplitude of the perturbation pressure depends on dD'/dz in the following fashion:

$$P'(z) = \varepsilon\bar{\rho}_d\frac{\Omega^2/k_x^2}{1-\Omega^2/(k_x^2\bar{c}^2)}\frac{dD'}{dz} \tag{27}$$

The remaining polarization relations are given in appendix B. The sum of the background vertical profiles and of the above-determined spatial and temporal fluctuations describes the thermodynamic state of the atmospheric medium whose microwave emission is measured by the radiometer.

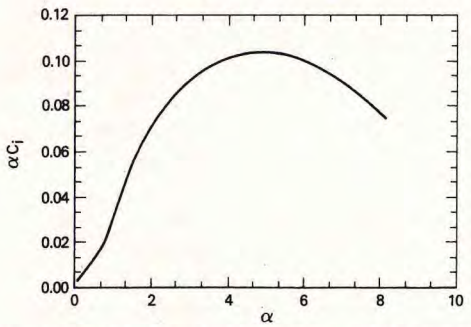

Fig. 13. Normalized growth rate $\alpha c_i = \omega_i H/V$ as a function of normalized wave number $\alpha = k_x H$. The values $H = 1000$ m and $V = 50$ m s^{-1} are the characteristic length and velocity for the system.

3. RESULTS

During February 2–4, 1984, time sequences of satellite cloud photographs, and measurements from an instrumented research aircraft, a surface array of microbarographs at the Boulder Atmospheric Observatory (BAO), the WPL radiometer at Stapleton Airport near Denver, Colorado, and other instruments, all revealed the presence of gravity wave activity in the troposphere. Time series of measured and derived quantities during this period are given in *Ciotti et al.* [1987].

We first concentrate our analysis on a 128-min segment of 2-min-averaged data starting at 1200 UTC, February 3, 1984, somewhat after the peak of the wave activity. As mentioned in section 2, we choose this time period mainly to minimize the contaminating effects of clouds when calculating brightness temperatures from the model. Later, we also analyze a 4-hour segment of data, starting at 1040 UTC, in part to compensate for the presence of nonstationarity in the system and in part to calculate the confidence limits of the data analysis to a higher level of accuracy.

Time series of the six brightness temperatures and the corresponding spectral density estimates are plotted in Figures 2 and 3, respectively. In Figure 4, the spectral density is given for the absolute pressure sensor located near the radiometer. The surface pressure spectrum reveals well-identified peaks around 6 and 10 hour^{-1}. We analyze in detail the peak at 6 hour^{-1} because for shorter periods the sampling rate is not adequate for a reliable spectral estimate. The brightness temperature spectra indicate distinct peaks around 8, 5, 6.5, 6, and 7 hour^{-1} for the radiometric frequencies of 20.6, 31.65, 52.85, 53.85, and 55.45 GHz,

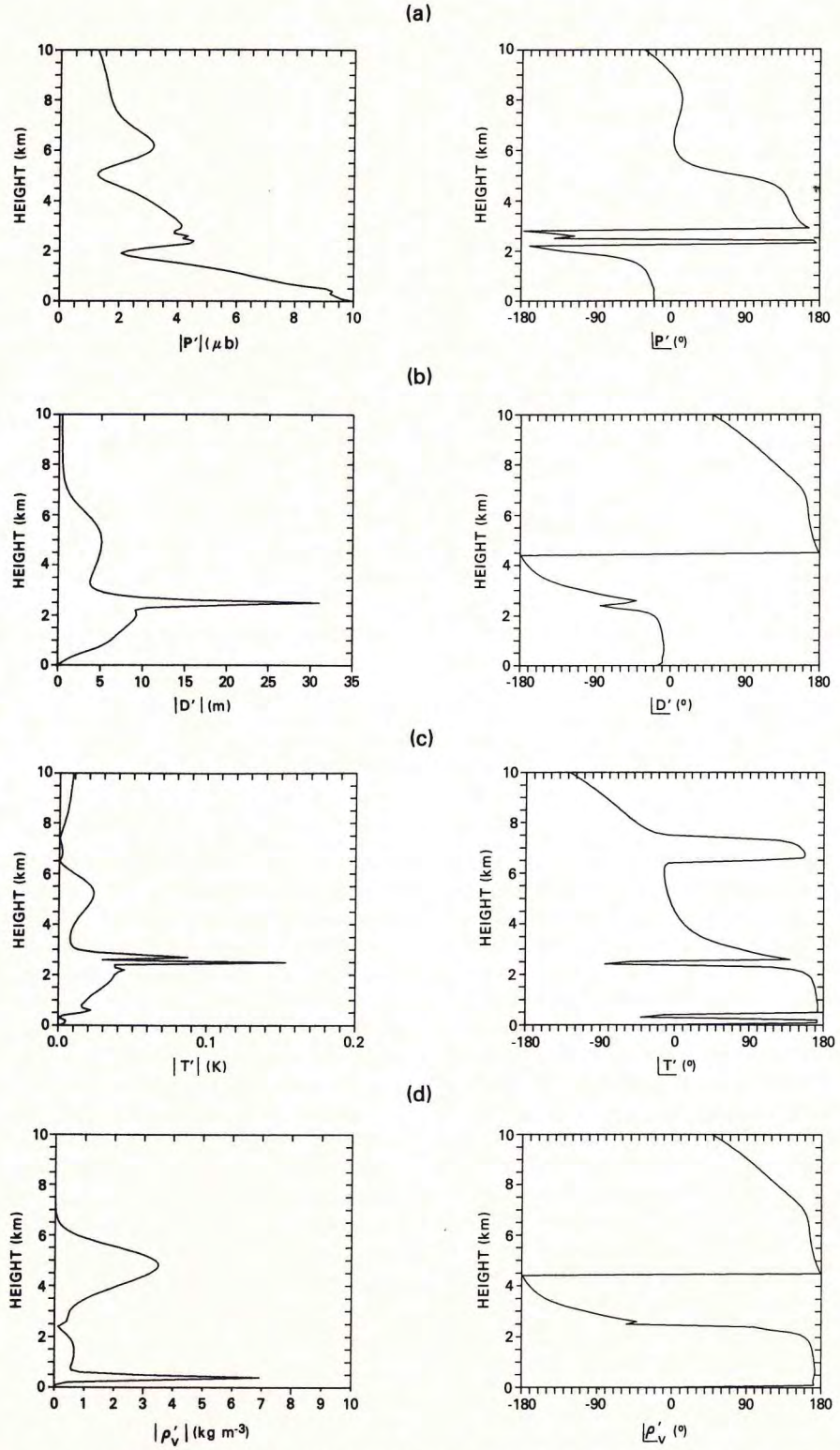

Fig. 14. Amplitude (left) and phase (right) of the (*a*) pressure, (*b*) vertical displacement, (*c*) temperature, and (*d*) water vapor density as a function of height for the wave with period $\tau = 593$ s, phase speed $c = 20.4$ m s^{-1}, and horizontal wavelength $\lambda = 12.1$ km.

respectively. The 58.8 GHz brightness temperature spectrum is rather flat around these frequencies. With the exception of 58.8 GHz, the width of each peak, as determined from an autoregressive spectral analysis, is approximately 2 hour^{-1}, which is less than the expected resolution bandwidth of 3.6 hour^{-1} of the Fourier spectral analysis. This close proximity of the peaks suggests that each brightness temperature measurement reflects the presence of the same disturbance that we assume, hereafter, to be centered at 6 hour^{-1}. In a spectral analysis of an earlier segment of data, 0832–1040 UTC on the same day, the situation was reversed between 55.45 and 58.8 GHz; that is, the 55.45 GHz record

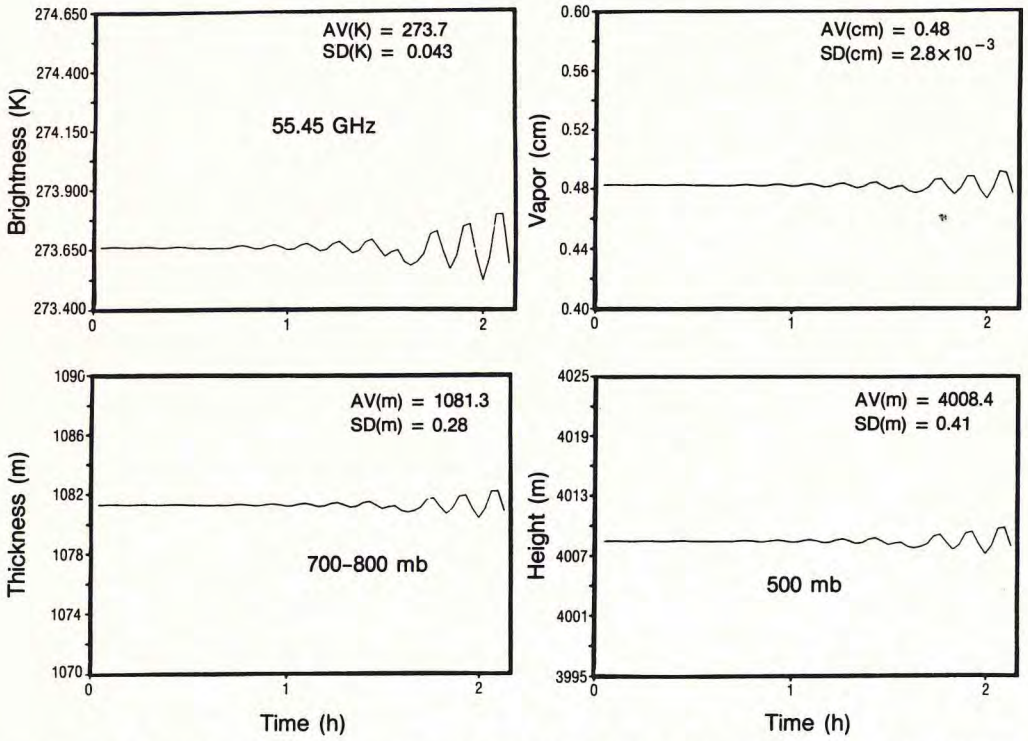

Fig. 15. Time series of brightness temperature at 55.45 GHz, 700–800 mb thickness, integrated water vapor, and 500-mb heights, derived from 2-min synthetic data that account for a gravity wave with a period of 593 s and a growth time constant of 1468 s. AV and SD are defined in the caption of Figure 2.

had no peaks, and the 58.8 GHz record had a pronounced one. This reversal indicates a certain amount of nonstationarity in the vertical level at which the disturbance occurs. We will return to the problem of nonstationarity when we analyze the 4-hour segment of data.

The information we derive from the network of differential microbarographs at the BAO is somewhat inconclusive. Spectral peaks at 555 and 454 s are present for several hours. However, the phase velocity vector (determined by cross correlation of four microbarograph signals), whose direction was consistently 330° from the north, had an amplitude that varied between 11 and 50 m s^{-1}, depending on the subintervals over which the cross-correlation was calculated.

Finally, for the period 1600–1846 UTC, an independent indication of the presence of disturbances was given by rapid-scan (every 5 minutes) satellite pictures in the visible spectrum that showed cloud structures with a spatial periodicity of about 10–15 km. One such a picture is reproduced in Figure 5*a*. These features persisted for several hours, propagated toward the southeast, and extended laterally toward the southwest as time progressed. The rapid-scan satellite pictures were obtained as part of an independent experiment on mountain waves which also involved the National Center for Atmospheric Research Sabreliner aircraft. A plot of the altitude of a segment of the flight path, roughly in the direction of wave propagation, is given in Figure 5*b* and confirms the wavelength observed by satellite.

In our data processing, geophysical quantities are derived from the brightness temperature observations by linear statistical inversion [*Strand and Westwater*, 1968]. Time series and spectra of various derived quantities confirm the presence of the 10-min spectral component. Time series of heights of constant pressure, thicknesses of atmospheric layers, and total water vapor content are plotted in Figures 6, 7, and 8, respectively. The corresponding spectra are displayed in Figures 9, 10, and 11. We note that, except for the 700-mb height and the precipitable water vapor, prominent peaks are present at 6 $hour^{-1}$. For the 700-mb height, the spectral density at 7 $hour^{-1}$ contains the hint of a peak; for the earlier segment of data at 0832–1040 UTC, the peak was much stronger. However, for both the 0832–1040 UTC and the 1200–1408 UTC time segments, the vapor peak was at ~8 $hour^{-1}$. As discussed above, this is considered to be within the resolution bandwidth of the 6 $hour^{-1}$ peak.

In summary, experimental evidence suggests the presence of a disturbance of 10-min period with spatial wavelength between 10 and 15 km and phase speed between 10 and 50 m s^{-1} in the 330° direction. Furthermore, the inversion technique used to retrieve the temperature profile and other quantities appears to retain the harmonic content of the measurements.

We seek an explanation of the origin of the disturbance in terms of a gravity wave generated by wind shear in the jet stream above the Denver area. Using data from the 1100 UTC February 3, 1984, rawinsonde launch from Denver and projecting the wind vector in various directions, we calculated the Richardson number

$$Ri\,(z) = n^2/(d\bar{u}/dz)^2 \tag{28}$$

and verified that height ranges existed where Ri dipped below 0.25. In particular, the direction of 315° was that of maximum shear with ranges of $Ri < 0.25$ about the levels of 500, 2500, and 7000 m. The wind $\bar{u}$ projected in the 315° direction, the temperature $\bar{T}$, and the dew point temperature (DPT) are plotted in Figure 12 as a function of height. For the

TABLE 1*a*. Measured and Calculated Standard Deviations of Both Clear Air and Cloudy Brightness Temperatures

Frequency, GHz	σ_{T_B}, K Measured	Calculated (Clear)	Calculated (Cloudy)
20.6	0.012 (0.009, 0.019)	0.021	0.024
31.65	0.028 (0.021, 0.043)	0.008	0.029
52.85	0.058 (0.044, 0.093)	0.010	0.037
53.85	0.049 (0.037, 0.078)	0.016	0.022
55.45	0.031 (0.023, 0.048)	0.016	0.016
58.8	0.023 (0.017, 0.036)	0.019	0.019

Measurement time: 1200–1408 UTC, February 3, 1984. Radiosonde release time: 1100 UTC, February 3, 1984. The 95% confidence limits (calculated from *Jenkins and Watts* [1969]) are shown after measured values. Cloud liquid amount, as derived from the 20.6 and 31.65 channels, equals 0.0006 mm.

lowest level (500 m) where $Ri < 0.25$, the values of $\bar{u}$ were too low to be of interest in the interpretation of the observations. We carried out the stability analysis of the atmospheric system to determine modes whose critical levels (i.e., the level where the horizontal phase velocity matches the mean wind $\bar{u}$ in amplitude and direction) fall within the remaining two height ranges.

The stability analysis consists of finding numerically the eigenvalues (k_x, ω) of (26) such that the corresponding eigenfunctions $D'(z)$ satisfy the condition of zero vertical velocity at the ground and the radiation condition at $z \to \infty$. To satisfy the latter, the system is capped by a layer with constant temperature and wind (see Figure 12). The radiation condition is imposed at 25 km, the height above which the effect of the disturbance on the measurements is negligible. Taking as initial guesses for λ and $\tau = 2\pi/\omega_r$ the value of 15 km and 10 min, respectively, we adopted a shooting method to find the eigenvalues: the guesses are updated for each integration of (26) that does not satisfy the proper boundary conditions to the chosen degree of accuracy [*Lalas and Einaudi*, 1976]. The profiles for $\bar{u}$ and $\bar{T}$ used to calculate the coefficients of (26) were a linear combination and hyperbolic tangent and gaussian functions chosen to interpolate the data in the least squares sense. The interpolated profiles are also plotted in Figure 12. This fitting has the advantage of producing a smooth profile in which the fluctuations due both to measurement errors and to the local perturbations are filtered out. Moreover, the analytic expression of the profile is continuous and continuously differentiable, both essential requirements of the model.

The results of the stability analysis are reproduced in Figure 13 for disturbances with a critical level of about 2500 m. Normalized growth rate $\omega_i H/V$ is plotted as a function of normalized wavenumber $\alpha = k_x H$, in the interval $\alpha = 0.1$–8. The quantities $H = 1000$ m and $V = 50$ m s^{-1} are characteristic spatial and velocity scales, respectively. The corresponding diagram for the nondimensional horizontal phase speed $\omega_r/(k_x V)$ versus α is essentially a horizontal line with $\omega_r/(k_x V) = 20.4$, which indicates that the system has very little dispersion. The results indicate that the atmospheric state can support a number of modes that grow exponentially in time and draw their energy from the kinetic energy of the jet.

Among these modes, we choose the one that corresponds to $\alpha = 0.52$. The associated period $\tau = 593$ s, horizontal wavelength $\lambda = 12.1$ km, and phase speed $c = \omega_r/k = 20.4$ m s^{-1} are well within the range of the observed values discussed earlier. Within limits, the choice of α is not critical. The imaginary part of the eigenvalue, $\omega_i = -6.8 \times 10^{-4}$ s^{-1}, corresponds to a growth time constant of 1468 s. In practice, the growth is not observed because the wave quickly settles into steady-state behavior brought about by nonlinear effects and/or dissipation. Linear theory often predicts well the main characteristics of the disturbances, wavelengths, and periods, which appear to persist past the linear stage. The vertical structure of the pressure, $D'(z)$, temperature, and water vapor density of the disturbance are reproduced in Figure 14. The effect of the critical level is clear, indicating that the largest influence on the measurements occurs around this height. However, these are not evanescent solutions which quickly go to zero away from the critical level. In fact, their effect is clearly present all the way to the Earth's surface. It should be noted that this mode does not correspond to a maximum of the growth rate. This is not unusual in atmospheric flows since the excitation of a particular mode may depend on a number of factors difficult to assess, such as horizontal inhomogeneities, time variations of the background state, orography, turbulence structure, and so on. Indeed, the stability analysis should not necessarily be viewed as a predictor for the observed wavelength, but rather as a means of obtaining the height variation and the relationships among the wave variables for a wave of the observed wavelength.

The stability analysis for those modes whose critical level is at about 7000 m above the surface was carried out and another solution was found whose λ, τ, and ω_r/k_x were within the measured values. Although a candidate, this solution was not found to be effective in explaining the

TABLE 1*b*. Partial Contribution to Calculated Brightness Temperatures

Frequency, GHz	σ_{T_B}, K Temperature	Water Vapor Density	Dry Density	Cloud Liquid Density	Total (Clear)	Total (Cloudy)
20.6	0.000	0.021	0.000	0.012	0.021	0.024
31.6	0.000	0.008	0.000	0.028	0.008	0.029
52.85	0.004	0.009	0.001	0.036	0.010	0.037
53.85	0.015	0.004	0.001	0.016	0.016	0.022
55.45	0.016	0.000	0.000	0.000	0.016	0.016
58.80	0.019	0.000	0.000	0.000	0.019	0.019

The weighting functions of Figure A1 were used in these calculations with a cloud liquid amount of 0.0006 mm.

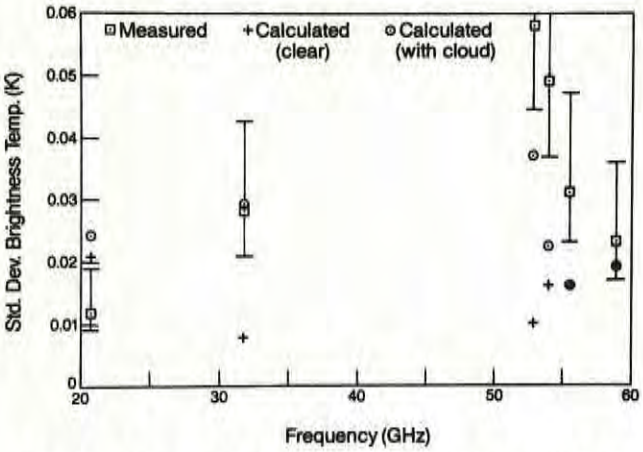

Fig. 16. Comparison of measured brightness temperature standard deviation with calculations for clear and for cloudy conditions for the period 1200–1408 UTC February 3, 1984. 95% confidence limits (calculated using the method of *Jenkins and Watts* [1969]) are shown together with measured values.

observations in the sense described below, probably because its level of generation was too high. We are not reproducing here the results of the stability analysis for these modes.

To test the validity of our model, synthetic data for the brightness temperature were constructed from (2). The input temperature, pressure, and water vapor were the superposition of the mean state and wavelike perturbations presented in section 2.1. Averages of the brightness temperatures over 2-min intervals were calculated to simulate the real data.

An example of time series of synthetic brightness temperature at 55.45 GHz is given in Figure 15. The graph displays the sinusoidal behavior and exponential growth of the gravity wave and, of course, does not display the complete harmonic content of the actual data. The lack of smoothness in the plots reflects the averaging process used to generate the 2-min synthetic samples. The nonlinear nature of (2) does not seem to affect the sinusoidal behavior very much, at least for a 128-min time interval. Also, the smoothing in height due to the finite width of the weighting function does not average out the fluctuations. The averaging out is not observed because the theoretical wavelength of the wave is large relative to the width of the weighting functions.

The 2-min averages of synthetic data are used in the same procedure that inverts the measurements and derives the heights of the constant pressure surfaces and the thicknesses of the atmospheric layers [*Strand and Westwater*, 1968]. This procedure is known as a priori statistical inversion and incorporates a history of radiosonde profiles with a physical radiative transfer model to provide a minimum variance estimate of profile parameters. Examples of the time series of the derived height, thickness, and of the integrated water vapor are shown in Figure 15.

To compare synthetic and measured spectra, it is necessary to isolate the power contained around the spectral peak at 6 hour^{-1} as given in Figure 3. This entails removing the background spectral density $S_{back}(\nu)$, presumably due to

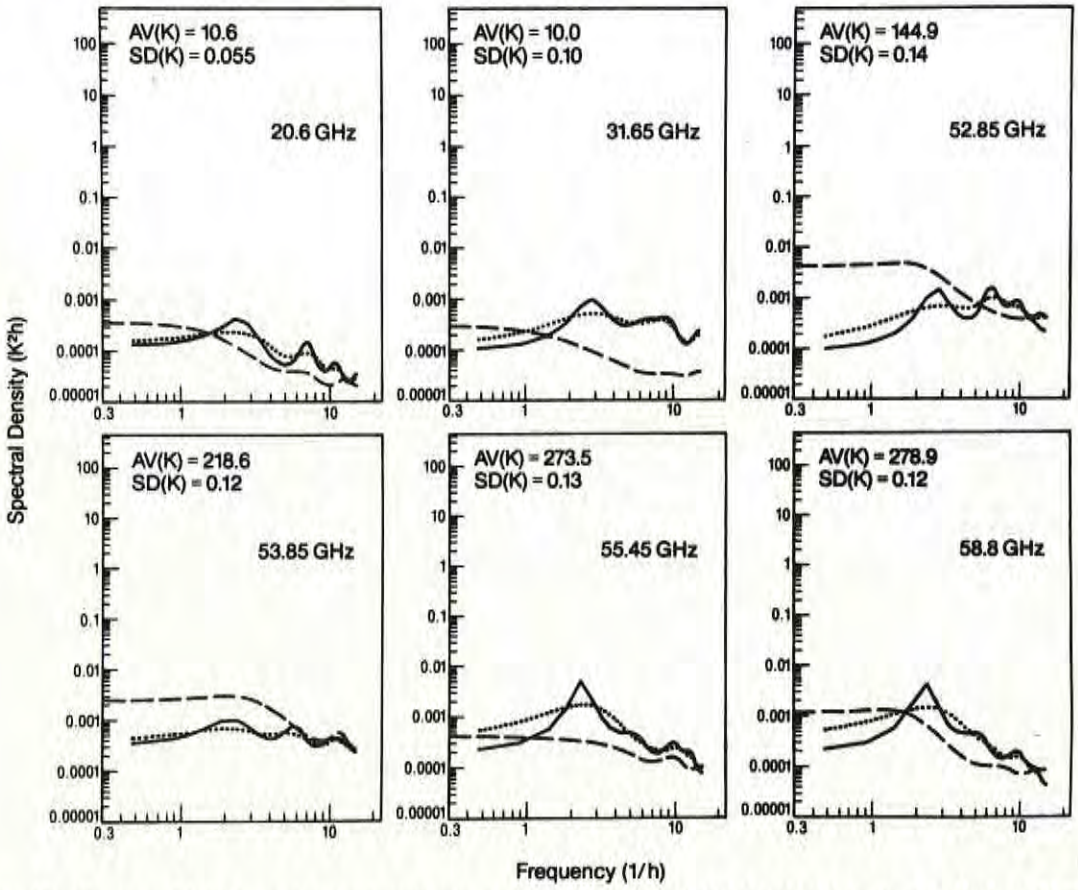

Fig. 17. Spectra of brightness temperature fluctuations for the period 1040–1448 UTC February 3, 1984. A 30-min running average was used to detrend the data. The figure legends are described in Figure 3.

turbulent fluctuations, from the measured spectral density $S_{meas}(\nu)$,

$$S_{meas}(\nu) = S_{back}(\nu) + S_{wave}(\nu) \quad (29)$$

where $S_{wave}(\nu)$ is the spectral density associated with the gravity wave. The integral of $S_{wave}(\nu)$ can be compared with the results of the gravity wave model. We determined $S_{wave}(\nu)$ as follows: we first fitted the background power spectral density $S_{back}(\nu)$ to a power law form

$$S_{back}(\nu) = \beta \nu^x \quad (30)$$

and determined the constants β and x from data outside the region of the spectral peak. Then we subtracted $S_{back}(\nu)$ from the measured maximum spectral density $S_{meas}(\nu)$ and integrated the resulting difference $[S_{meas}(\nu) - S_{back}(\nu)]$ by numerical quadrature. This procedure gave the resulting standard deviation σ

$$\sigma^2 = 2 \int_{\nu_1}^{\nu_2} [S_{meas}(\nu) - S_{back}(\nu)]\, d\nu \quad (31)$$

In Table 1*a*, we initially compared measured and calculated spectra of brightness temperatures. The latter are normalized to be consistent with a measured pressure standard deviation of 27 μb. These comparisons agreed roughly within a factor of 2 to 5. We noticed that except for the 20.6 GHz channel, measured fluctuations were substantially greater than the calculated ones. In order to investigate the origin of the discrepancies, we first investigated the effect on the fluctuations of cloud liquid water at 20.6, 31.65, 52.85, and 53.85 GHz. From the 20.6 and 31.65 GHz channels, we estimated a cloud liquid amount of 0.0006 mm around the spectral peak at 6 hour^{-1}. This amount could represent, as an example, a cloud liquid density of 0.0012 g/m^3 distributed over a height interval of 500 m. Using this amount with the cloud liquid weighting functions of Figure A1, the cloud contributions to the brightness temperatures were estimated and the corrected values reproduced in Table 1*a* for comparison. In addition, we show in Table 1*b* the partial contributions to brightness temperatures from all four of the relevant atmospheric variables. In Figure 16 we also show

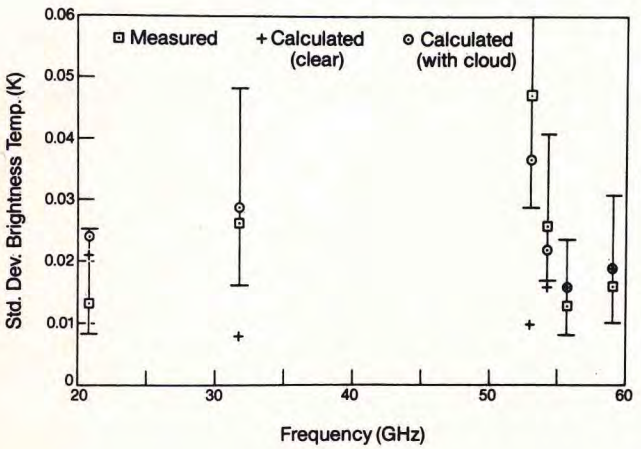

Fig. 18. Comparison of measured brightness temperature standard deviation with calculations for clear and cloudy conditions for the period 1040–1448 UTC February 3, 1984. 95% confidence limits are shown together with the measured values.

TABLE 2. Measured and Calculated Standard Deviations of Both Clear and Cloudy Brightness Temperatures

Frequency, GHz	σ_{T_B}, K Measured	Calculated (Clear)	Calculated (Cloudy)
20.6	0.013 (0.008, 0.025)	0.021	0.024
31.65	0.026 (0.016, 0.048)	0.008	0.029
52.85	0.047 (0.029, 0.084)	0.010	0.037
53.85	0.026 (0.017, 0.041)	0.016	0.022
55.45	0.013 (0.008, 0.024)	0.016	0.016
58.8	0.016 (0.010, 0.031)	0.019	0.019

Measurement time: 1040–1448 UTC, February 3, 1984. 30-mm running average used to detrend data. Radiosonde release time: 1100 UTC, February 3, 1984. The 95% confidence intervals are given after measurements. Cloud liquid amount, as derived from the 20.6 and 31.65 GHz channels, equals 0.0006 mm.

plots of the measured and calculated total power. It is evident that the introduction of clouds improves substantially the correspondence between measurements and calculations which now agree within a factor of at least 2.2. At the same time, however, only two of the six calculated points fell within the 95% confidence limits, although two others were close.

Another possible source of discrepancy between measured and synthetic data is the nonstationary nature of the atmospheric state. Indeed, nonstationarity became evident when we repeated the spectral analysis for 128-min segments of data for every 20 minutes starting from 1040 UTC to 1330 UTC. It was obvious from the spectral plots that both the center frequencies and the total power varied from period to period, particularly for the 55.45 and 58.80 GHz channels. To partially account for the effect of nonstationarity, as well as to improve the significance of the confidence limits of the calculations, we then detrended the entire data set by using a 30-min running average, and performed the analysis for the period 1040–1448 UTC. For this time interval, all spectra exhibited peaks around 6 hour^{-1} and the amplitudes were in much better agreement with the calculations that included clouds. For this interval too, a spectral analysis showed a cloud liquid amount of 0.0006 mm around the spectral peak at 6 hour^{-1}. The spectral densities for these data are shown in Figure 17 and the corresponding comparisons of total power are shown in Figure 18 and Table 2. It is now apparent, after both the inclusion of clouds in the calculations and after suitable detrending of the measurements, that all the calculations with clouds fall well within the 95% confidence limits. Conversely, for the frequencies sensitive to clouds, i.e., the first four channels, only one falls within the required confidence limits for the clear calculations.

After having convinced ourselves of satisfactory agreement between measurements and calculations, we proceeded to retrieve quantities from the measured data.

In Tables 3 and 4, we compare radiometrically measured quantities with those determined from the synthetic data for both the 1200–1408 UTC and the 1040–1448 UTC time intervals. We remind the reader that the latter time interval was detrended with a running 30-min average. With the exception of the 700–800 mb thickness and the quantities above 500 mb, the calculated values are close to or within the 95% confidence interval for the detrended data. The discrepancies in the 700–800 mb thickness occur in a region

TABLE 3. Measured and Calculated Standard Deviation σ of Geopotential Height h and Precipitable Water Vapor V

	σ_1, Measured	σ_2, Measured	σ, Calculated
h (700 mb)	0.03 (0.02, 0.09)	0.07 (0.04, 0.13)	0.06
h (500 mb)	0.91 (0.5, 2.3)	0.52 (0.32, 0.97)	0.29
h (300 mb)	2.86 (1.58, 7.39)	1.61 (0.99, 2.99)	0.44
V, cm	4.0×10^{-3} (3.4×10^{-3}, 1.0×10^{-2})	2.0×10^{-3} (1.2×10^{-3}, 3.7×10^{-3})	2.0×10^{-3}

Measurement time for σ_1: 1200–1408 UTC; for σ_2: 1040–1446 UTC, February 3, 1984. The 95% confidence limits are written in parentheses after the measured quantities. Radiosonde release time: 1100 UTC, February 3, 1984. Units for h are meters.

where the radiometric temperature retrievals generally have good accuracies. As was previously mentioned, nonstationarity is present in all channels, but is particularly strong for the 55.45 and 58.80 GHz channels, which are the two most significant ones in the 700–800 mb retrievals. Since the spectra of our detrended data represent an average, we believe this lowering of peak values by the averaging process to be the principal cause of this disagreement. The disagreement above 500 mb probably represents the lack of sensitivity of the radiometer to changes occurring above that level. The remaining quantities show excellent agreement between model and detrended data.

4. Conclusions

We have presented in this paper a detailed analysis of the dependence of radiometric measurements on the presence of an internal gravity wave superimposed on a mean atmospheric state. We demonstrate the plausibility of using radiometers to detect fluctuating components in the atmospheric temperature and humidity. We use a perturbation analysis in which we express brightness temperature fluctuations measured at the ground as vertical integrals of wave components of temperature, dry air density, cloud liquid density, and water vapor density, each multiplied by the appropriate weighting functions. The weighting functions depend on mean quantities only. The variables are assumed to fluctuate because of internal gravity waves generated by wind shear in a background system which is dynamically unstable except near the critical levels.

A direct comparison between measured and model-generated brightness temperatures generally confirms the oscillations measured on 3 February 1984 can be described qualitatively and quantitatively in terms of such waves. However, in the comparisons, agreement was obtained only by including the affects of clouds and by suitable detrending of the data.

We also demonstrated that the retrieval algorithm used in deriving from the radiometer data the precipitable water vapor, surfaces of constant pressure, and layer thicknesses agrees quite well with the prediction of the model.

Since the vertical structure of the waves presented here their amplitudes, periods, and horizontal wavelengths are commonly observed [*Einaudi et al.*, 1989], we expect radiometric measurements to be often affected by these disturbances. Moreover, we suggest that the radiometer can be used as an important tool to investigate not only the mean atmospheric state, but its dynamic evolution as well.

Appendix A: Derivation of Equation (12)

The optical depth can be written as follows with the use of a Taylor expansion:

$$\tau_\nu(0, s) = \bar{\tau}_\nu(0, s) + \tau'_\nu(0, s) + \text{higher-order terms} \quad \text{(A1)}$$

with

$$\bar{\tau}_\nu(0, s) = \int_0^s \bar{\alpha}_\nu(s')\, ds'$$

$$\tau'_\nu(0, s) = \int_0^s \alpha'_\nu(s')\, ds' \quad \text{(A2)}$$

where $\bar{\alpha}_\nu$ and α'_ν are given by (8) and (9), respectively. Similar expressions can be written for $\bar{\tau}(0, \infty)$ and $\tau'_\nu(0, \infty)$. The use of the Taylor expansion

$$\exp[-\tau_\nu(0, s)] = \exp[-\bar{\tau}_\nu(0, s)][1 - \tau'_\nu(0, s)] + \text{higher-order terms} \quad \text{(A3)}$$

without the higher-order terms, allows us to rewrite (2) as

$$T_{b\nu} = \bar{T}_{b\nu} + T'_{b\nu} \quad \text{(A4)}$$

TABLE 4. Measured and Calculated Standard Deviations σ of Geopotential Thicknesses Δh

	σ_1, Measured	σ_2, Measured	σ, Calculated
Δh (700–800 mb)	0.43 (0.24, 1.35)	0.13 (0.08, 0.24)	1.59
Δh (600–700 mb)	0.51 (0.31, 1.3)	0.25 (0.16, 0.49)	0.20
Δh (500–600 mb)	0.69 (0.39, 1.71)	0.41 (0.25, 0.76)	0.14
Δh (300–500 mb)	0.75 (0.42, 3.34)	1.11 (0.68, 2.06)	0.16
Δh (500–800 mb)	0.99 (0.57, 2.49)	0.58 (0.34, 1.16)	0.53

Same times as in Table 3. The 95% confidence limits are written in parentheses after the measured quantities. Units for Δh are meters.

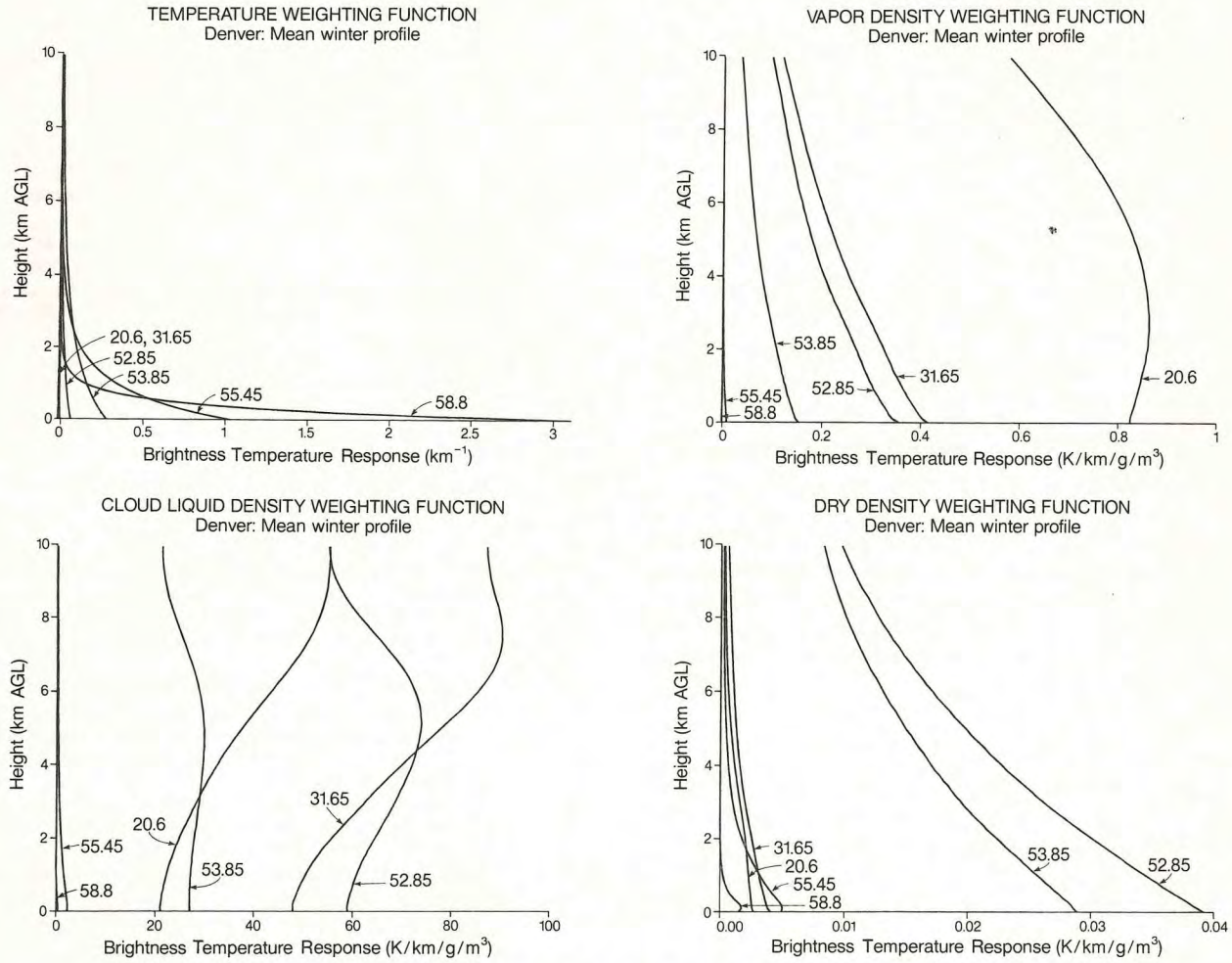

Fig. A1. Weighting functions for temperature, water vapor, dry air density, and liquid water density. These functions were generated from a 10-year climatological mean (1971–1980) for the months of December, January, and February at Denver, Colorado. They are shown primarily to illustrate the sensitivity of the brightness temperatures to various atmospheric parameters. They were used to calculate the partial contribution from each of the four relevant atmospheric variables reproduced in Table 1*b*.

where

$$\bar{T}_{b\nu} = T_b^{(\mathrm{ext})} \exp\left[-\bar{\tau}_\nu(0, \infty)\right] + \int_0^\infty \bar{T}(s)\bar{\alpha}_\nu(s) \exp\left[-\bar{\tau}_\nu(0, s)\right] ds \qquad \text{(A5)}$$

and

$$T'_{b\nu} = -T_b^{(\mathrm{ext})} \exp\left[-\bar{\tau}_\nu(0, \infty)\right] \int_0^\infty \alpha'_v(s)\, ds + \int_0^\infty \exp\left[-\bar{\tau}_\nu(0, s)\right] \left(-\bar{\alpha}_\nu \bar{T} \int_0^s \alpha'_\nu\, ds' + \bar{\alpha}_\nu T + \bar{T}\alpha'_\nu\right) ds \qquad \text{(A6)}$$

The inversion of the order of integration leads to the following identity:

$$\int_0^\infty \left(\exp\left[-\bar{\tau}_\nu(0, s)\right]\bar{\alpha}_\nu(s)\bar{T}(s) \int_0^s \alpha'_\nu(s')\, ds'\right) ds = \int_0^\infty \left(\exp\left[-\bar{\tau}_\nu(0, s)\right]\alpha'_\nu(s) \int_s^\infty \cdot \exp\left[-\bar{\tau}_\nu(s, s')\right]\bar{T}(s')\bar{\alpha}_\nu(s')\, ds'\right) ds \qquad \text{(A7)}$$

With the use of (A7), we can write the perturbation brightness temperature measured at the ground as

$$T'_{b\nu} = \int_0^\infty \left[W_T(s)T'(s) + W_{\rho_d}(s)\rho'_d(s) + W_{\rho_v}(s)\rho'_v(s) + W_{\rho_c}(s)\rho'_c(s)\right] ds \qquad \text{(A8)}$$

where

$$W_T(s) = \bar{\alpha}_\nu(s) \exp[-\bar{\tau}_\nu(0, s)] + \left(\frac{\partial \bar{\alpha}_\nu}{\partial T}\right) \exp[-\bar{\tau}_\nu(0, s)] \cdot \left(\bar{T}(s) - T_b^{(\text{ext})} \exp[-\bar{\tau}_\nu(s, \infty)] - \int_s^\infty \bar{T}(s')\bar{\alpha}_\nu(s') \exp[-\bar{\tau}_\nu(s, s')]\, ds'\right) \quad \text{(A9)}$$

$$W_{\rho_d}(s) = \left(\frac{\partial \bar{\alpha}_\nu}{\partial \rho_d}\right) \exp[-\bar{\tau}_\nu(0, s)]\left[\bar{T}(s) - T_b^{(\text{ext})} \exp[-\bar{\tau}_\nu(s, \infty)] - \int_s^\infty \bar{T}(s')\bar{\alpha}_\nu(s') \exp[-\bar{\tau}_\nu(s, s')]\, ds'\right] \quad \text{(A10)}$$

and W_{ρ_v} or W_{ρ_c} are the same as W_{ρ_d} when ρ_v or ρ_c replace ρ_d. Equation (A8) is the same as (12). The partial derivatives are evaluated for the mean state. The weighting functions are plotted as a function of height in Figure A1. They were generated from a 10-year climatological mean (1971–1980) for the months of December, January, and February at Denver, Colorado.

Appendix B: Polarization Relations

We reproduce here the polarization coefficients relating U', T', R_d', and R_v' to D' and dD'/dz. The polarization coefficient for P' is given by (27).

Horizontal wind

$$U'(z) = \frac{\varepsilon\Omega/k_x}{1 - \Omega^2/(k_x^2\bar{c}^2)} \frac{dD'}{dz} - \varepsilon \frac{d\bar{u}}{dz} D' \quad \text{(B1)}$$

Temperature

$$T'(z) = -\bar{T}\frac{\varepsilon}{g} n^2 D' + \frac{\varepsilon}{c_p} \frac{\Omega^2/k_x^2}{1 - \Omega^2/(k_x^2\bar{c}^2)} \frac{dD'}{dz} \quad \text{(B2)}$$

Dry air density

$$R_d'(z) = \bar{\rho}_d \varepsilon \frac{n^2}{g} D' + \bar{\rho}_d \varepsilon \frac{\Omega^2/(k_x^2\bar{c}^2)}{1 - \Omega^2/(k_x^2\bar{c}^2)} \frac{dD'}{dz} \quad \text{(B3)}$$

Water vapor density

$$R_v'(z) = \varepsilon\bar{\rho}_\nu \left(\frac{n^2}{g} + \frac{1}{\bar{\rho}_d}\frac{d\bar{\rho}_d}{dz} - \frac{1}{\bar{\rho}_v}\frac{d\bar{\rho}_v}{dz}\right) D' + \bar{\rho}_v \varepsilon \frac{\Omega^2/(k_x^2\bar{c}^2)}{1 - \Omega^2/(k_x^2\bar{c}^2)} \frac{dD'}{dz} \quad \text{(B4)}$$

Acknowledgments. This work was supported in part by NSF Grant ATM 8213784. F. Canavero was supported in part by a grant of the Italian Ministry of Education. The authors acknowledge the useful comments on the manuscript by Earl Gossard. The comments of two anonymous reviewers added substantially to the paper. In addition, Susan Caplan performed the extensive processing required to obtain Figure 5*a*. We are also grateful for the assistance of F. Hoelzl. We acknowledge the use of aircraft data provided by the National Center for Atmospheric Research. One of the authors (A.J.B.) was supported in part by FAF contract DTFA01-84-Z-02007 and acknowledges the encouragement of B. Colamosca of the Federal Aviation Administration.

References

Augustine, J. A., and E. J. Zipser, The use of wind profilers in a mesoscale experiment, *Bull. Am. Meteorol. Soc.*, *68*, 4–17, 1987.

Balsley, B. B., and K. S. Gage, On the use of radars for operational wind profilers, *Bull. Am. Meteorol. Soc.*, *63*, 1009–1018, 1982.

Beard, C. I., and L. U. Martin, Microwave radiometric sensing of the marine boundary layer, *Radio Sci.*, *13*, 291–301, 1978.

Chimonas, G., The extension of the Miles-Howard theorem to compressible fluids, *J. Fluid Mech.*, *43*, 833–836, 1970.

Ciotti, P., E. R. Westwater, M. T. Decker, A. J. Bedard, Jr., and B. B. Stankov, Ground-based microwave radiometric observations of the temporal variation of atmospheric geopotential height and thickness, *IEEE Trans. Geosci. Remote Sens.*, *GE-25*, 600–615, 1987.

Decker, M. T., F. Einaudi, and J. J. Finnigan, The influence of gravity waves on radiometric measurements: A case study, *J. Appl. Meteorol.*, *20*, 1231–1238, 1981.

Einaudi, F., and D. P. Lalas, The propagation of acoustic gravity waves in a moist atmosphere, *J. Atmos. Sci.*, *30*, 365–376, 1973.

Einaudi, F., A. J. Bedard, Jr., and J. J. Finnigan, A climatology of gravity waves and other coherent disturbances at the Boulder Atmospheric Observatory during March–April 1984, *J. Atmos. Sci.*, *46*, 303–329, 1989.

El-Raey, M., Remote sensing of atmospheric waves in O_2 and H_2O microwave emissions, *Radio Sci.*, *17*, 766–772, 1982.

Hines, C. O., and D. W. Tarasick, On the detection and utilization of gravity waves in airglow studies, *Planet. Space Sci.*, *35*, 851–866, 1987.

Hogg, D. C., M. T. Decker, F. O. Guiraud, K. B. Earnshaw, D. A. Merritt, K. P. Moran, W. B. Sweezy, R. G. Strauch, E. R. Westwater, and C. G. Little, An automatic profiler of the temperature, wind and humidity in the troposphere, *J. Appl. Meteorol.*, *22*, 807–831, 1983*a*.

Hogg, D. C., F. O. Guiraud, and E. R. Westwater, Emission measurements of 31.6 GHz absorption by atmospheric water vapor, *Radio Sci.*, *18*, 1295–1300, 1983*b*.

Jenkins, G. M., and D. G. Watts, *Spectral Analysis and Its Applications*, 525 pp., Holden-Day, San Francisco, Calif., 1969.

Lalas, D. P., and F. Einaudi, On the stability of a moist atmosphere in the presence of a background wind, *J. Atmos. Sci.*, *30*, 795–800, 1973.

Lalas, D. P., and F. Einaudi, On the characteristics of gravity waves generated by atmospheric shear layers, *J. Atmos. Sci.*, *33*, 1248–1259, 1976.

Liebe, H. J., Modeling attenuation and phase of radio waves in air at frequencies below 1000 GHz, *Radio Sci.*, *16*, 1183–1199, 1981.

Liou, K.-N., *An Introduction to Atmospheric Radiation*, 392 pp., Academic, San Diego, Calif., 1980.

Strand, O. N., and E. R. Westwater, Minimum rms estimation of the numerical solution of a Fredholm integral equation of the first kind, *SIAM J. Numer. Anal.*, *5*, 287–295, 1968.

Strauch, R. G., D. A. Merritt, K. P. Moran, K. B. Earnshaw, and D. van de Kamp, The Colorado wind-profiling network, *J. Atmos. Oceanic Tech.*, *1*, 37–49, 1984.

Ulaby, F. T., R. K. Moore, and A. K. Fung, Microwave remote sensing: Active and passive, in *Microwave Remote Sensing Fundamentals and Radiometry*, vol. I, edited by D. S. Simonett, 456 pp., Addison-Wesley, Reading, Mass., 1981.

Westwater, E. R., Wang Z., N. C. Grody, and L. M. McMillin, Remote sensing of temperature profiles from a combination of observations from the satellite-based microwave sounding unit and the ground-based profiler, *J. Atmos. Oceanic Tech.*, *2*, 97–109, 1985.

A. J. Bedard, Jr., M. J. Falls, J. A. Schroeder, and E. R. Westwater, Wave Propagation Laboratory, National Oceanic and Atmospheric Administration, Boulder, CO 80303.

F. G. Canavero, Dipartimento di Elettronica, Politecnico of Turin, Turin 10129, Italy.

F. Einaudi, Laboratory for Atmospheres, NASA Goddard Space Flight Center, Greenbelt, MD 20771.

(Received December 9, 1988;
revised November 7, 1989;
accepted November 7, 1989.)